RSC Advances

ROYAL SOCIETY OF CHEMISTRY

www.rsc.org/advances

RSC Advances

RSCPublishing

ARTICLE

Synthesis and characterization of $BiPO_4$/g-C_3N_4 nanocomposites with significantly enhanced visible-light photocatalytic activity for Benzene degradation

Cite this: DOI: 10.1039/xoxxoooooox

Received ooth January 2012,
Accepted ooth January 2012

DOI: 10.1039/xoxxoooooox

www.rsc.org/

Xuejun Zou[a], Yuying Dong[a], Zhaobo Chen[a*], Dapeng Dong[c], Dongxue Hu[a], Xinyong Li[b*], Yubo Cui[a]

In order to enhance the photocatalytic activity of g-C_3N_4 under visible light region, the $BiPO_4$/g-C_3N_4 nanocomposites photocatalysts with different $BiPO_4$ contents were prepared through hydrothermal with calcination method. Throgh N_2 adsorption-desorption measurement, the $BiPO_4$/g-C_3N_4 showed large surface area (234.8 m^2 g^{-1}) and small pore diameter and the incorporation of $BiPO_4$ caused a red-shift of g-C_3N_4 in visible light region by UV-vis diffuse reflection spectroscopy. The photocatalytic degradation of benzene over $BiPO_4$/g-C_3N_4 was investigated. The degradation of benzene could get 73% in 2 wt% $BiPO_4$/g-C_3N_4 photocatalysts under optimum reaction conditions, which was 6 times compared with pure g-C_3N_4 at the same conditions. The improved photoactivity of $BiPO_4$/g-C_3N_4 could be ascribed to its effective separation of photogenerated hole-electron pairs between $BiPO_4$ and g-C_3N_4. Furthermore, the $BiPO_4$/g-C_3N_4 photocatalysts showed excellent stability. By using the *in situ* FTIR technique, ethyl acetate, carboxylic acid and aldehyde could be regarded as the intermediate products, and CO_2 and H_2O were produced as the final products. Through Electron spin resonance (ESR), $OH\cdot$ and $O_2\cdot^-$ were examined in the photocatalytic degradation of benzene.

Introduction

The effective applications on solar energy conversion and environmental pollutions removal by semiconductor photocatalysts have attracted considerable attention in modern society[1-4]. In the past decade, traditional photocatalyst TiO_2 has still been extensively investigated owing to its merits, such as the nontoxicity, low cost and excellent stability against photocorrosion[5-8]. However, it can only be acivated by the ultraviolet light ($\lambda < 400$ nm), which only constitutes about 4% of the solar spectrum, due to its wide bandgap (anatase 3.4 eV) and have low seperation efficiency of electron-hole pairs formed in photocatalytic processes[7]. Therefore, it is necessory to fabricate efficient new types of photocatalysts responed to visible light in order to improve the utilization of solar energy[9-11].

Recently, graphitic carbon nitride (g-C_3N_4), which is as organic semiconductor materials, are increasing interest due to the constructed plastic optoelectronic systems and the chemical structure of organic semiconductor materials since Wang et al. reported that g-C_3N_4 showed a good photocatalytic performance for hydrogen or oxygen product by water splitting under visible light irradiation[12]. For g-C_3N_4, the catalysts possess high stability respect to thermal and chemical attacks due to its tri-striazine ring structure and high condensation. Meanwhile, it features a semiconductor band gap of 2.7 eV corresponding to an optical wavelength of 460 nm, which belongs to visible light region[13]. With an attractive electronic structure, g-C_3N_4 is an ideal semiconductor and is valuable for photocatalysis driven applications. According to the literatures[14-17], the conduction band (CB) of g-C_3N_4 is located at about -1.3 V vs. NHE (pH = 7). Whereas its valence band (VB) top locates at about 1.4 V, resulting in a small thermodynamic driving force for organic pollutants oxidation. Furthermore, the photocatalytic efficiency of bulk g-C_3N_4 is limited due to fast recombination of electron-hole pairs formed in photocatalytic process. In order to resolve this problem, several routes have been used including non-metal doping (boron[18], fluorine[19] and sulfur[20]), optimizing porous structure[17], and coupling g-

C_3N_4 with semiconductor[21, 22]. In these methods, there is a great interest in heterostructure of semiconductor catalytic performance. Through the coupling, synergistic effect may be achieved. High utilization efficiency of solar light can be achieved by the narrow band gap semiconductor[15, 23]. Simultaneously, high seperation rate of photoinduced electrons-hole pairs can be realized due to the interaction of the two semiconductors. Bismuth salt photocatalysts (such as Bi_2WO_6[24]), which reported by other groups, exhibited superior photocatalytic activity for the pollutions degradation. $BiPO_4$, as one of them, finds applications in catalysis and can be used for separating radioactive elements[25, 26]. PO_4^{3-}, which possesses a large negative charge, is postulated to help the electron-hole pairs separation, which plays an important role in its excellent photocatalytic activity.

Benzene is regarded as the priority hazardous substance due to its high toxicity, confirmed carcinogenicity, and environmental persistence because it is widely used as a solvent in industrial processes[27-30]. Therefore, how to effectively remove benzene from the ambient environment is necessary by mild technology.

Herein, we synthesized a new inorganic-organic $BiPO_4$/g-C_3N_4 nanocomposites photocatalysts by hydrothermal with simple calcination method. It was found the photodegradation activity of $BiPO_4$/g-C_3N_4 for benzene was greatly enhanced under visible light irradiation comparing with the pure g-C_3N_4. And the $BiPO_4$/g-C_3N_4 nanocomposites photocatalyst show excellent stability during the photochemical reactions. The mechanism for this enhanced photocatalytic benzene degradation can be ascribed to the large surface area, strong absorption in visible light and excellent charge transfer between $BiPO_4$ and g-C_3N_4 based on the photoluminescence results.

Experimental section

All chemicals were used as received without any further modification. $Bi(NO_3)_3{\cdot}5H_2O$, $NaH_2PO_4{\cdot}2H_2O$, Melamine and anhydrous ethanol were purchased from Tianjin Kermel Chemical Reagents Development Centre. The distilled water was used in experimental process.

Photocatalysts preparation

$BiPO_4$ was synthesized by hydrothermal process. Typically, 8 mmol of $Bi(NO_3)_3{\cdot}5H_2O$ was soluted into 160 mL distilled water under magnetic stirring. Then 28.8 mmol $NaH_2PO_4{\cdot}2H_2O$ was added into the mixture and stirred for 1 h. The resulting suspension was transferred into a Teflon-lined stainless steel autoclave and maintained at 160 °C for 24 h. The products were washed three times with distilled water and anhydrous ethanol respectively before it dried at 120 °C for 8 h.

$BiPO_4$/g-C_3N_4 with different amount of $BiPO_4$ was synthesized by calcination method. In a typical procedure, $BiPO_4$ (0.016, 0.036, 0.048 and 0.065 for sample 1 wt% Bi-CN, 2 wt% Bi-CN, 3 wt% Bi-CN and 4 wt% Bi-CN, respectively) was dissolved in 2 mL of anhydrous ethanol, and then 15.8 mmol melamine was added and dispersed by ultrasonic for 5 min. The mixtures were dried at 85 °C overnight to remove ethanol. Subsequently, the as prepared mixtures were put into a crucible with cover and heated to 500 °C for 2 h with a heating rate of 20 °C min^{-1} and 520 °C for another 2 h in a muffle furnace. The pure g-C_3N_4 was also prepared for comparison purpose.

Characterization

The crystal structure of the samples was investigated by X-ray diffraction (XRD) using a powder X-ray diffractometer (LabX-6000, Shimadzu, Japan, λ = 1.5406 Å) with a scan rate of 0.02° s^{-1} over a 2θ range from 20 to 70°. The morphology of the samples was detected by using transmission electron microscopy (TEM; JEOL JEM-2100; accelerating voltage, 200 kV). UV–vis diffuse reflection spectra were recorded on a Shimadzu UV-500 spectrophotometer, using $BaSO_4$ as reference. The pore structure of the obtained sample was characterized by N_2 adsorption using an adsorption apparatus (Quantachrome NOVA Instruments V 2.2 gas sorption analyzer). Specific surface area of the samples was determined from the Brunauer-Emmett-Teller (BET) equation, and pore volume was determined from the total amount adsorbed at relative pressures near unity. The photoluminescence (PL) spectra were surveyed by an Edinburgh FL/FS900 spectrophotometer. The electron spin resonance (ESR) signals of the radicals trapped by 5, 5-dimethyl-1-pyrroline N-oxide (DMPO) were detected at ambient temperature with a Bruker (E500) spectrometer. The irradiation source was a Quanta-Ray Nd: YAG pulsed laser system (λ = 532 nm, 10 Hz). The settings for the ESR spectrometer were as follows: center field = 3510 G; sweep width = 200 G; microwave frequency = 9.85 GHz; modulation frequency = 100 kHz and power = 20 mW. To minimize measurement errors, the same quartz capillary tube was used throughout the ESR measurements.

Photocatalytic activity test

The photocatalytic degradation of gaseous benzene was carried out under visible light, using a 500W Xe lamp (Shanghai Seagull Colored Optical Glass Co., Ltd.) with a UV-cutoff filter (λ > 400 nm). Photocatalytic degradation of benzene was conducted in a Pyrex glass cylindrical reactor with the volume of 120 mL. 0.1 g of the catalysts was put at the bottom of the reactor. Then, benzene vapor was mixed with the air (78% nitrogen, 21% oxygen as reaction gas) and introduced into the reactor at room temperature. Once the concentration of the reactants had

been stabilized, the inlet and outlet ports were shut off. After adsorption equilibration in the dark for 1 h, the lamp was turned on to allow the photoreaction to proceed. The concentration of benzene was analyzed by gas chromatogram (Agilent7890A) with HP-5 capillary column (30 m×320 μm×0.25 μm).

The *in situ* FTIR measurement was carried out in a home-built IR cell (about 120 mL), equipped with two NaCl windows and a sample holder for the catalyst wafer to analyze the degradation mechanism of benzene. Benzene vapor mixture with the dry air, which pretreated through a drying column packed with desiccant and molecular sieves, was introduced to the IR cell at room temperature. When the sample was saturated with reaction gas, the inlet and outlet ports were shut off. After adsorption equilibration in the dark for 1 h, the 500 W Xe lamp (Shanghai Seagull Colored Optical Glass Co.) with a UV-cutoff filter ($\lambda > 400$ nm) were used as visible light. A Bruker VERTEX 70 FT-IR equipped with a DTGS detector was employed for recording of the FTIR spectra.

Results and discussion

Characterization of the $BiPO_4$/g-C_3N_4 nanocomposites

XRD pattern is used to investigate the phase structures of the samples, and the typical diffraction patterns are shown in Fig. 1. The peak at 27.4° in the XRD patterns of the samples is due to the stacking of the conjugated aromatic system, which is indexed for graphitic materials as the (002) peak of the g-C_3N_4[13]. For $BiPO_4$, Evidently, the same diffraction peaks of $BiPO_4$ (JCPDS 15-0766) have been detected, in which the peaks at 25.5°, 29.5°, 31.3°, 41.9° and 48.7° are corresponding to the diffraction peaks of (110), (200), (102), (211) and (212) crystal planes of $BiPO_4$[31]. For $BiPO_4$/g-C_3N_4 samples, these peaks are intensified with the increasing amount of $BiPO_4$, while the ones belonging to C_3N_4 gradually decreased. The intensity of the peak is decreased which indicated that $BiPO_4$ nanoparticles may be wrapped in the interlayer of g-C_3N_4 and weaken the force of interlayer stacking, accordingly. In addition, no impurity peaks were observed.

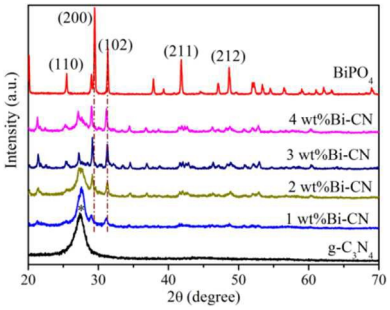

Fig 1. XRD patterns of the $BiPO_4$, pure g-C_3N_4 and Bi-CN.

Fig. 2 shows a comparison of the FTIR spectra of $BiPO_4$, pure g-C_3N_4 and Bi-CN samples. In the case of $BiPO_4$, 1 032 cm^{-1} and 596 cm^{-1} could be attributed to $\delta(PO_4)$ and $\nu(PO_4)$, respectively[32]. For the g-C_3N_4, the broad band at 3 155 cm^{-1} is attributed to stretching modes of NH and NH_2.The band at 1 325 cm^{-1} corresponds to C(sp2)–N stretching, and the band at 1 641 cm^{-1} assigns to C(sp2)=N stretching modes. The 807 cm^{-1} band is attributed to s-triazine ring vibration modes. The C–NH–C unit is found in melem (1 252 and 1 325 cm^{-1})[33]. It can be clearly seen that the main characteristic peaks of g-C_3N_4 and $BiPO_4$ all appeared in the Bi-CN photocatalysts.

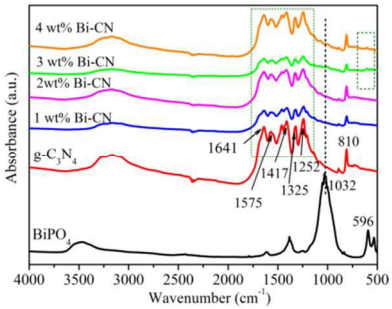

Fig 2. FTIR spectra of the $BiPO_4$, pure g-C_3N_4 and Bi-CN.

The existence of $BiPO_4$ in the g-C_3N_4 was visualized by the TEM observations, as shown in Fig. 3. The g-C_3N_4 shows layer structure (Fig. 3a and b), which is consistent with results reported previously. $BiPO_4$ nanoparticles with average size of about 20 nm were well dispersed in the g-C_3N_4 phase (Fig. 3c). The HRTEM reveals that the fringe spacing of 0.326 nm can be indexed to the (002) crystal planes of g-C_3N_4 (Fig. 3d), while the lattice spacing of 0.210 nm can be assigned to the (200) facets of $BiPO_4$.

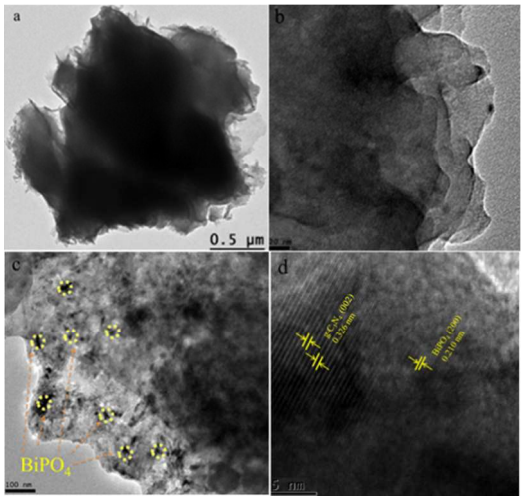

Fig 3. TEM images of pure g-C_3N_4 (a and b) and 2 wt% Bi-CN (c) and HRTEM image (d) of 2 wt% Bi-CN.

Fig. 4 shows N_2 adsorption-desorption isotherms of the 2 wt% Bi-CN and pure g-C_3N_4. The 2 wt% Bi-CN and pure g-C_3N_4 were found to be of IV-type isotherms according to the BDDT classification. The hysteresis loops for the 2 wt% Bi-CN and g-C_3N_4 were similar, which

shown the incorporation of $BiPO_4$ didn't affect the specific surface area of g-C_3N_4. The BET surface areas of the 2 wt% Bi-CN and g-C_3N_4 were 234.8 and 232.6 m^2 g^{-1}, respectively (see Table 1). The large surface area can provide more photocatalytic active sites and will be beneficial for the photocatalytic application. Meanwhile, the pore size of 2 wt% Bi-CN was calculated as 2.432 nm based on the N_2 adsorption-desorption isotherms, exhibiting a character of mesoporous materials. It has been reported that large pore volume might be beneficial for the catalytic activity, while a small average pore diameter might also be one of the reasons for the increasing catalytic activity[34, 35].

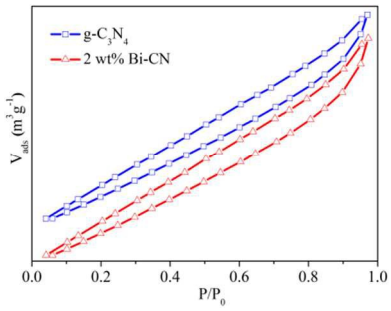

Fig 4. N_2 adsorption-desorption isotherms of 2 wt% Bi-CN and pure g-C_3N_4.

Table 1 Physical properties of 2 wt% Bi-CN and g-C_3N_4.

Catalyst	Surface Area (m^2/g)	Pore Volume (m^3/g)	Average Pore Diameter (nm)
2 wt% Bi-CN	234.8	0.301	2.432
g-C_3N_4	232.6	0.286	2.441

Fig. 5a-5f shows the XPS spectra of 2 wt% Bi-CN. Fig. 5a is the XPS survey spectrum of the sample which contains the peaks of Bi 4p, Bi 4d, Bi 4f, Bi 5d, O KLL, O 1s, P 2s, P 2p, N 1s, and C 1s. The peaks at 164.9 eV and 159.6 eV can be assigned to the binding energies of Bi 4f 5/2 and Bi 4f 7/2 (Fig. 5b), which indicates the existence of a trivalent oxidation state for Bi[36]. A broad signal peak at about 132.7 eV suggests that the P in the sample exist in the oxidation state of P^{5+} (Fig. 5c)[33]. For the O 1s, the peak at 530.9 eV is attributed to the crystal lattice oxygen, while the peak at 532.6 eV is related to adsorbed oxygen (Fig. 5d). The binding energy of 288.2 eV can be corresponded to the C-N-C coordination in the C 1s (Fig. 5e). In the N 1s spectrum several binding energies can be separated (Fig. 5f). The main signal shows occurrence of C–N–C groups (398.7 eV) and tertiary nitrogen N–$(C)_3$ groups (400.7 eV)[37].

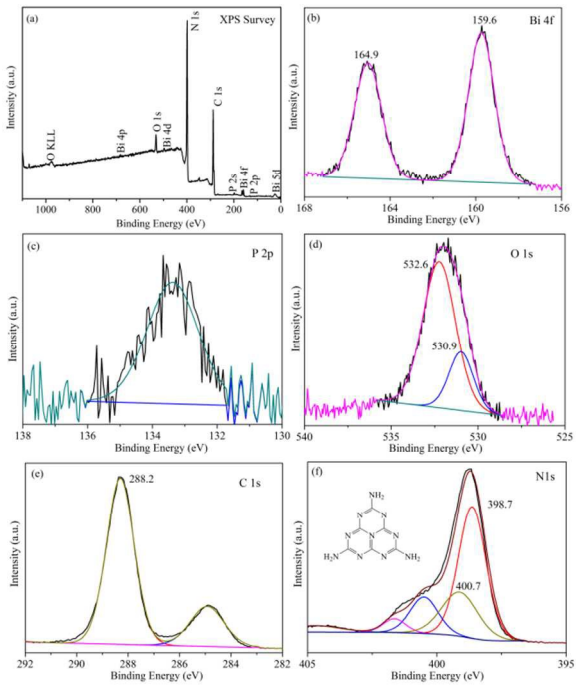

Fig 5. XPS survey spectrum of 2 wt% Bi-CN (a) and its high-resolution XPS spectra: (b) Bi 4f, (c) P 2p, (d) O 1s, (e) C 1s and (f) N 1s.

The absorption range of light plays an important role in the photocatalysis, especially for the visible light photodegradation of contaminants. Fig 6a shows the UV-vis DRS of the as-synthesized samples. As it can be observed, $BiPO_4$ only can absorb UV light, which absorbance region is from 257 to 368 nm. However, for pure g-C_3N_4 and Bi-CN samples, strong absorption in the visible region can be appeared, which absorbance region is from 371 to 465 nm and Bi-CN samples exhibit absorption edge of 571 nm together with an increased light absorption, which has a significant redshift (ca. 106 nm) compared with g-C_3N_4. The results indicated that loading of $BiPO_4$ improved the light absorption ability. There are two major reasons to explain the resultd. Firstly, the interaction of heterojunction between $BiPO_4$ and g-C_3N_4 effectively enhances the separation of electron-hole pairs account for the band gap transition of photo-generated electrons and then enhanced the absorption in the visible light region[31]. Secondly, as a colour change of the composites samples, which become darker, that is, from pale yellow to grey, along with a increasing amount of $BiPO_4$ was introduced into the g-C_3N_4 would also cause the absorbance enhanced[38]. The band gap of the pure g-C_3N_4 is estimated to be about 2.7 eV (Fig 6b). It is noteworthy that the band gap of Bi-CN samples, which is from 2.3 to 2.5 eV due to incorporation different amount of $BiPO_4$, tends to be smaller than that of pure g-C_3N_4, indicating that the absorption of the Bi-CN samples is shifted to the lower energy region.

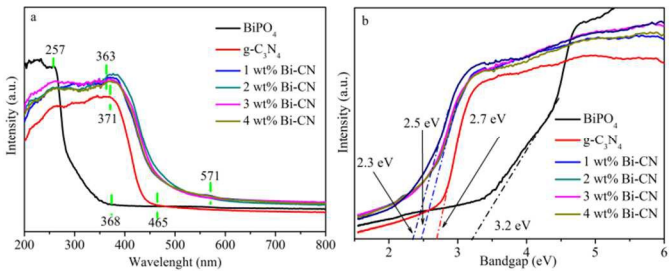

Fig 6. UV-visible DRS spectra (a) and curves of $(\alpha h\nu)^{1/2}$ vs. photon energy (b) of the $BiPO_4$, pure g-C_3N_4 and Bi-CN with different amount of $BiPO_4$.

Photocatalytic degradation performance of the $BiPO_4$/g-C_3N_4 photocatalysts

The photocatalytic degradation of gaseous benzene over the $BiPO_4$/g-C_3N_4 photocatalysts was illustrated in Fig. 7a. As shown in Fig. 7a, the photocatalytic activities of $BiPO_4$ and g-C_3N_4 were very low under visible light. The conversion of benzene was only 2% and 11%, respectively. In contrast, Bi-CN samples presented much higher photo degradation activity for benzene under the same conditions. Especially, the conversion of benzene over 2 wt% Bi-CN achieved 73% after 4 h under visible light irradiation. The Bi-CN exhibit a higher photocatalytic activity for the decomposition of gaseous benzene compared to pure g-C_3N_4 under visible light irradiation, which is due to its strong absorption in visible-light region (from 571 to 363 nm) and excellent charge separation characteristics. However, the removal of benzene decreased with increasing amount of $BiPO_4$, which might result from the additional recombination of photo induced electron-hole pairs in the excess amount of $BiPO_4$ particles and decreasing the diffraction intensity assigned to g-C_3N_4 because the crystal had important role in photocatalytic oxidation process[39, 40].

The photocatalytic reaction followed a pseudo-first-order reaction, and the rate constant of benzene decomposition over 2 wt% Bi-CN, which was estimated to be about 0.316 h^{-1}, was faster than the other samples (Fig. 7b). Furthermore, the photochemical stability of 2 wt% Bi-CN was tested. As shown in Fig. 7c, the benzene degradation efficiency declines only about 8% after four consecutive runs. Therefore, the as-synthesized $BiPO_4$/g-C_3N_4 photocatalyst exhibits excellent stability in the visible light photochemical degradation reactions.

The PL spectroscopy is usually utilized to investigate the seperation of the photogenerated electron-hole pairs during photocatalytic process[41, 42]. Fig. 7d shows the PL spectra of g-C_3N_4 and Bi-CN. The PL spectrum of g-C_3N_4 shows a strong emission, which indicates the electrons and holes recombine rapidly. By contrast, for Bi-CN photocatalysts, there was weak PL peak observed, indicating that the photogenerated electron-hole pairs recombination was very slow. It is concluded that the heterojunction of $BiPO_4$ and g-C_3N_4 may act as an active center for decreasing the recombination of photoinduced electron-hole pairs. On the other hand, according to the result of the N_2 adsorption-desorption, Bi-CN showed large specific surface area, which means that its surface can provide more photocatalytic active sites.

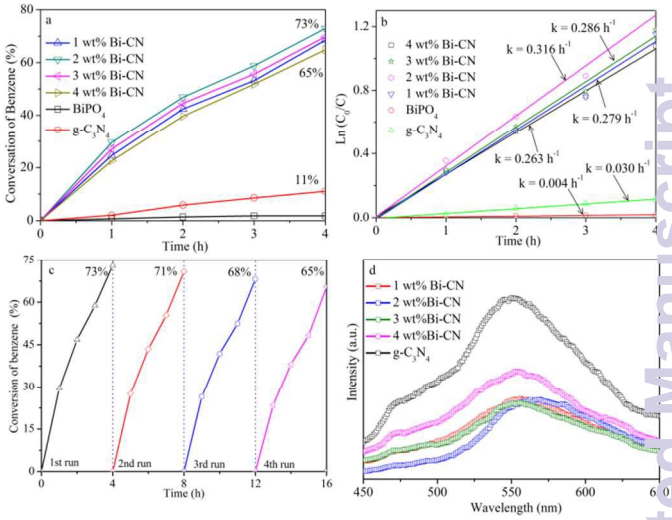

Fig. 7. (a) Photocatalytic degradation of benzene using the as-prepared the $BiPO_4$, pure g-C_3N_4 and Bi-CN photocatalysts 1-5 ($[benzene]_0$ = 115 ppm, $[catalysts]_0$ = 100 mg, I_0 = 200 mW cm^{-2}). (b) The variation of ln (C/C_0) of benzene by different processing routes. (c) Cyclic photodegradation of benzene over 2 wt% Bi-CN under visible light irradiation. (d) PL spectra of g-C_3N_4 and Bi-CN.

In situ FTIR study of photodegradation mechanism of benzene

Real-time monitoring of transient events occurring on the catalyst during the reaction and the surface adsorbed species, which were detected by *in situ* FTIR, will give an important insight into the reaction mechanisms. In this work, a set of IR transmittance spectra are obtained during the photocatalytic oxidation of benzene over 2 wt% Bi-CN (Fig. 8). Prior to light irradiation (t=0), when benzene reached adsorption equilibrium on the surface of the 2 wt% Bi-CN, strong peaks due to gas-phase benzene appeared at 3 090, 3 055 and 3 047 cm^{-1}, which are assigned to the C-H stretching mode of benzene, respectively[43] (Fig. 8a). The band of 1 483 cm^{-1} is associated with C=C stretching. The vibrational bands at 1 804, 1 820, 1 951, and 1 966 cm^{-1} are assigned to C-H out-of-plane bending mode[44] (Fig. 8c). The bands at 1 050, 1 038 and 1 025 cm^{-1} could be ascribed to C-H in-plane deformation vibrations[43] (Fig. 8d). After reaction, the intensity of bands at 3 090, 3 055 and 3 047 cm^{-1} decreased significantly with increasing reaction

time. After 4 h, most of benzene was decomposed. Meanwhile, the bands at 2 360 and 2 342 cm^{-1} (Fig. 8b) corresponding to CO_2 increased as the reaction proceeded, and some new surface species, which appeared at 1 109, 949 and 791 cm^{-1}, were evidenced by the FTIR spectra in Fig. 8d. Among them, bands at 1 109 cm^{-1} is assigned to the C-O-C stretching vibration which existed in ester[45]. The 949 cm^{-1} band is assigned to O-H out-of-plane deformation vibration of carboxylic acid, and 791 cm^{-1} is assigned to C-H deformation vibration of aldehyde[46]. On the basis of the previous reports and the results, ethylacetate, carboxylic acid and aldehyde are the intermediate products during the photocatalytic degradation of benzene, CO_2 and H_2O are produced as the final product.

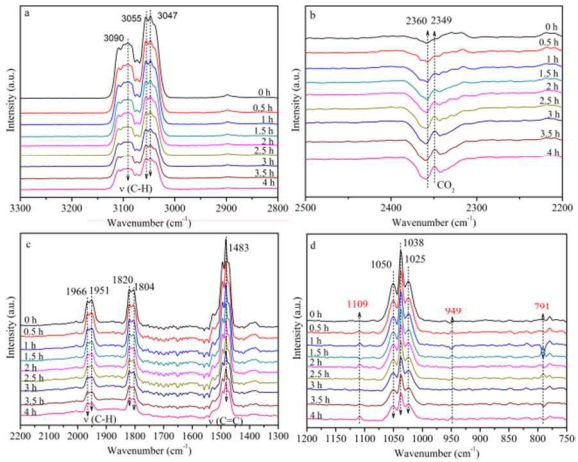

Fig. 8. (a-d) Infrared spectra recorded as a function of irradiation time following the photooxidation of toluene over 2 wt% Bi-CN photocatalyst.

In order to detect the reactive species evolved during the photocatalytic reaction process, such as hydroxyl radical and superoxide radical species, the electron spin resonance (ESR) technique was usually used[47]. As shown in Fig. 9a, four characteristic peaks of DMPO-OH· with intensity 1:2:2:1 can be observed with visible light irradiated aqueous dispersions of 2 wt% Bi-CN. Similarly, the stronger six characteristic peaks of the DMPO-O_2·$^-$ adducts are also observed with visible light irradiated methanol dispersions of 2 wt% Bi-CN in Fig 9b. ESR results indicate that the generation of OH· radical and O_2·$^-$ radical species is crucial during the reaction and it is confirmed that both OH· and O_2·$^-$ radicals are produced on the surface of 2 wt% Bi-CN and OH· radicals with strong oxidation capability act as the predominant species.

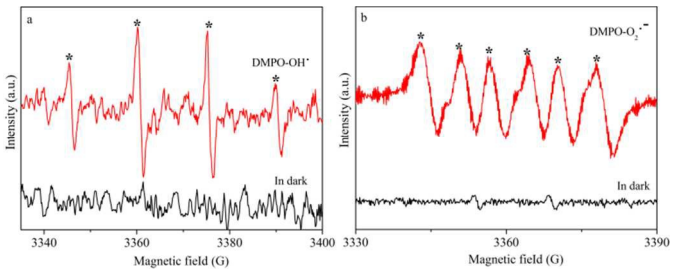

Fig. 9. ESR spectra of radical adducts trapped by DMPO in 2 wt% Bi-CN dispersions after 60 s visible-light irradiation (λ > 400 nm): (a) DMPO-OH· formed in irradiated aqueous dispersions; (b) DMPO-O_2·$^-$ formed in irradiated methanol dispersions.

Based on the above results, the photocatalytic mechanism may be proposed in Scheme 1. Under visible light irradiation, electrons (e^-) are excited from the VB of g-C_3N_4 and created holes (h^+) in the VB. Normally, these charge carriers quickly recombine and only a fraction of electrons could participate in the photocatalytic reaction. However, when g-C_3N_4 is connected with $BiPO_4$ to form composites, these photoinduced electrons on the CB of g-C_3N_4 tend to transfer to $BiPO_4$ particles due to their excellent electronic conductivity, improving to hole-electron separation. The transferred electrons will accumulate on the $BiPO_4$ nanoparticles and presumably as interface bound exciton pairs to capture the adsorbed O_2 and H_2O on g-C_3N_4 surface to form OH· and O_2·$^-$, and then participate in photocatalytic oxidation reaction. Meanwhile, on the VB of g-C_3N_4, the high separation efficiency of photogenerated electron–hole pairs is result in the increase of the number of holes, which could directly enhance the moderate performance of mineralization ability.

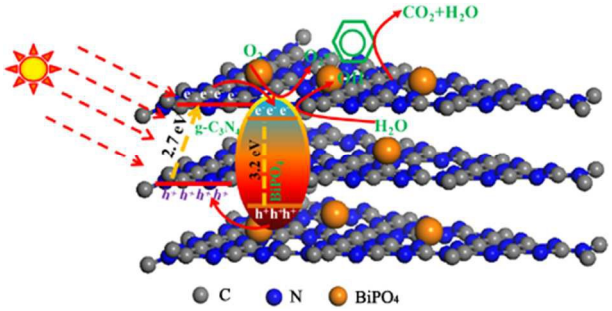

Scheme. 1. Schematic diagram showing the possible mechanism for the photocatalytic degradation of benzene over the $BiPO_4$/g-C_3N_4.

Conclusions

In summary, we have successfully synthesized $BiPO_4$/g-C_3N_4 by hydrothermal with calcination method for efficient photocatalytic degradation of gaseous benzene under visible light irradiation. The photocatalytic activities of $BiPO_4$/g-C_3N_4 on benzene degradation under visible light irradiation increase to about 6.0 times as high as

those of pure g-C_3N_4. The significant enhancement on photocatalytic performance was ascribed to strong absorption in visible light and rapid photogenerated electron transfer rate and charge separation efficiency in $BiPO_4$/g-C_3N_4. Through *in situ* FTIR technique, phenol, carboxylic acid and aldehyde could be regarded as the intermediate products, and CO_2 and H_2O are determined as the final product during the reaction process. Through ESR, $OH\cdot$ and $O_2\cdot^-$ are examined in the photocatalytic degradation of benzene. Such $BiPO_4$/g-C_3N_4 nanocomposites with high photocatalytic performances may provide an alternative of traditional catalysts to address energy conversion, green chemistry, and environmental issues.

Acknowledgements

This work was supported financially by the National Nature Science Foundation of China (No. 21477001, No. 21301023, No. 51208131 and No. 51278088), Liaoning province high school program for excellent talents (second levels), Dalian Science and Technology Fund (2013J21DW016), National rural areas supporting science-technology project of China (No. 2013BAJ12B02) and special grand national science-technology project (No. 2014ZX07204-005, 2012ZX07201003-002). The authors are grateful to the Institute of Environmental Biotechnology in Dalian Nationalities University for their technical and logistic assistance.

Notes and references

[a] *Department of Environmental Science and Technology, Dalian Nationalities University, Dalian, 116600, China. Email: zhaobochen@dlnu.edu.cn; Tel: +86-8765-6347; Fax: +86-8765-6347.*

[b] *State Key Laboratory of Fine Chemical and Key Laboratory of Industrial Ecology and Environmental Engineering, School of Environmental Sciences and Technology, Dalian University of Technology, Dalian, 116024, China. E-mail address: xyli@dlut.edu.cn; Tel.: +86-411-8470-7733; Fax: +86-411-8470-7733.*

[c] *School of Physics and Materials Engineering, Dalian Nationalities University, Dalian 116600, PR China*

References

1. C. T. Dinh, H. Yen, F. Kleitz and T. O. Do, *Angew Chem Int Ed Engl*, 2014, 53, 6618-6623.
2. G. Manna, R. Bose and N. Pradhan, *Angew Chem Int Ed Engl*, 2014, 53, 6743-6746.
3. J. Tian, Z. Zhao, A. Kumar, R. I. Boughton and H. Liu, *Chem Soc Rev*, 2014, 43, 6920-6937.
4. X. Wang, G. Sun, P. Routh, D. H. Kim, W. Huang and P. Chen, *Chem Soc Rev*, 2014, 43, 7067-7098.
5. H.-E. Kim, J. Lee, H. Lee and C. Lee, *Applied Catalysis B: Environmental*, 2012, 115-116, 219-224.
6. M. Pelaez, N. T. Nolan, S. C. Pillai, M. K. Seery, P. Falaras, A. G. Kontos, P. S. M. Dunlop, J. W. J. Hamilton, J. A. Byrne, K. O'Shea, M. H. Entezari and D. D. Dionysiou, *Applied Catalysis B: Environmental*, 2012, 125, 331-349.
7. R. Asahi, T. Morikawa, H. Irie and T. Ohwaki, *Chem Rev*, 2014, 114, 9824-9852.
8. K. Lee, A. Mazare and P. Schmuki, *Chem Rev*, 2014, 114, 9385-9454.
9. J. L. Wang, C. Wang and W. Lin, *ACS Catalysis*, 2012, 2, 2630-2640.
10. M. L. Marin, L. Santos-Juanes, A. Arques, A. M. Amat and M. A. Miranda, *Chem Rev*, 2012, 112, 1710-1750.
11. D. Chen, H. Zhang, Y. Liu and J. Li, *Energy & Environmental Science*, 2013, 6, 1362-1387.
12. X. Wang, K. Maeda, A. Thomas, K. Takanabe, G. Xin, J. M. Carlsson, K. Domen and M. Antonietti, *Nat Mater*, 2009, 8, 76-80.
13. X. Bai, L. Wang, Y. Wang, W. Yao and Y. Zhu, *Applied Catalysis B: Environmental*, 2014, 152-153, 262-270.
14. Z. a. Huang, Q. Sun, K. Lv, Z. Zhang, M. Li and B. Li, *Applied Catalysis B: Environmental*, 2015, 164, 420-427.
15. M. J. Muñoz-Batista, M. Fernández-García and A. Kubacka, *Applied Catalysis B: Environmental*, 2015, 164, 261-270.
16. L. Ge, C. C. Han, X. L. Xiao and L. L. Guo, *Applied Catalysis B: Environmental*, 2013, 142, 414-422.
17. S. Cao and J. Yu, *The Journal of Physical Chemistry Letters*, 2014, 5, 2101-2107.
18. S. C. Yan, Z. S. Li and Z. G. Zou, *Langmuir*, 2010, 26, 3894-3901.
19. Y. Wang, Y. Di, M. Antonietti, H. Li, X. Chen and X. Wang, *Chemistry of Materials*, 2010, 22, 5119-5121.
20. G. Liu, P. Niu, C. H. Sun, S. C. Smith, Z. G. Chen, G. Q. (Max) Lu, and H. M. Cheng, *J. Am. Chem. Soc.* 2010, 132, 11642-11648.
21. J. Chen, S. Shen, P. Guo, M. Wang, P. Wu, X. Wang and L. Guo, *Applied Catalysis B: Environmental*, 2014, 152-153, 335-341.
22. Y. He, J. Cai, L. Zhang, X. Wang, H. Lin, B. Teng, L. Zhao, W. Weng, H. Wan and M. Fan, *Industrial & Engineering Chemistry Research*, 2014, 53, 5905-5915.
23. S. Zhou, Y. Liu, J. M. Li, Y. Y. Wang, G. Y. Jiang, Z. Zhao, D. X. W, A. J. Duan, J. Liu and Y. C. Wei, *Applied Catalysis B: Environmental*, 2014, 158-159, 20-29.
24. L. Ge, C. Han and J. Liu, *Applied Catalysis B: Environmental*, 2011, 108-109, 100-107.
25. G. Liu, S. Liu, Q. Lu, H. Sun and Z. Xiu, *Industrial & Engineering Chemistry Research*, 2014, 53, 13023-13029.
26. Y. Liu, Y. Lv, Y. Zhu, D. Liu, R. Zong and Y. Zhu, *Applied Catalysis B: Environmental*, 2014, 147, 851-857.
27. T. Marino, R. Molinari and H. García, *Catalysis Today*, 2013, 206, 40-45.
28. H. Zhuang, Q. Gu, J. Long, H. Lin, H. Lin and X. Wang, *RSC Advances*, 2014, 4, 34315-34324.
29. F. Villanueva, A. Notario, J. A. Adame, M. C. Millan, R. Mabilia and J. Albaladejo, *Environ Technol*, 2013, 34, 289-299.
30. D. K. Ortega-Gonzalez, D. Zaragoza, J. Aguirre-Garrido, H. Ramirez-Saad, C. Hernandez-Rodriguez and J. Jan-Roblero, *Folia Microbiol (Praha)*, 2013, 56, 569-577.
31. Z. Li, B. Li, S. Peng, D. Li, S. Yang and Y. Fang, *RSC Advances*, 2014, 4, 35144-35188.
32. B. Long, J. Huang and X. Wang, *Progress in Natural Science: Materials International*, 2012, 22, 644-653.
33. Z. Li, S. Yang, J. Zhou, D. Li, X. Zhou, C. Ge and Y. Fang, *Chemical Engineering Journal*, 2014, 241, 344-351.
34. C. Andriamiadamanana, C. Laberty-Robert, M. T. Sougrati, S. Casale, C. Davoisne, S. Patra and F. Sauvage, *Inorg Chem*, 2014, 53, 10129-10139.
35. M. Tahir, C. Cao, N. Mahmood, F. K. Butt, A. Mahmood, F. Idrees, S. Hussain, M. Tanveer, Z. Ali and I. Aslam, *ACS Appl Mater Interfaces*, 2014, 6, 1258-1265.
36. W. C. Xu, G. Y. Zhou, J. Z. Fang, Z. Liu, Y. F. Chen and C. P. Cen, *Int. J. Photoenergy*, 2013, 234806
37. S. Wang, D. Li, C. Sun, S. Yang, Y. Guan and H. He, *Applied Catalysis B: Environmental*, 2014, 144, 885-892.
38. J. Yuan, Q. Gao, X. Li, Y. Liu, Y. Fang, S. Yang, F. Peng and X. Zhou, *RSC Adv.*, 2014, 4, 52332-52337.
39. C. Xiong, X. Deng and J. Li, *Applied Catalysis B: Environmental*, 2010, 94, 234-240.
40. C.-Y. Yue, X.-W. Lei, R.-Q. Liu, H.-P. Zhang, X.-R. Zhai, W.-P. Li, M. Zhou, Z.-F. Zhao, Y.-X. Ma and Y.-D. Yang, *Crystal Growth & Design*, 2014, 14, 2411-2421.
41. Y. Ren, Q. Zhao, X. Li, W. Xiong, M. Tade and L. Liu, *Journal of Nanoparticle Research*, 2014, 16, 2532.
42. T. Simon, N. Bouchonville, M. J. Berr, A. Vaneski, A. Adrovic, D. Volbers, R. Wyrwich, M. Doblinger, A. S. Susha, A. L. Rogach, F.

Jackel, J. K. Stolarczyk and J. Feldmann, *Nat Mater*, 2014, 13, 1013-1018.
43. S.V. Awate, R. K. Sahu, M. D. Kadgaonkar, R. Kumar and N. M. Gupta, *Catal. Today*, 2009, 141, 144-151.
44. W. C. Wu, L. F. Liao, C. F. Lien and J. L. Lin, *Phys. Chem. Chem. Phys.*, 2001, 3, 4456-4461.
45. H. P. Yang, R. Yan, H. P. Chen, D. H. Lee, D. T. Liang and C.G. Zheng, *Energy Fuels*, 2006, 20, 1321-1328.
46. N. Sivasankar and S. Vasudevan, *J. Phys. Chem. B* 2004, 108, 11585-11590.
47. F. Dong, Z. Y. Wang, Y. H Li, W. K. Ho and S. C. Lee, *Environ. Sci. Technol.* 2014, 48, 10345-10353.